IEEE Access
Multidisciplinary ⋮ Rapid Review ⋮ Open Access Journal

Received May 31, 2019, accepted July 2, 2019, date of publication July 11, 2019, date of current version July 29, 2019.

Digital Object Identifier 10.1109/ACCESS.2019.2928179

Analysis and Optimization of Multi-Winding Toroidal Inductors for Use in Multilayered Technologies

N. VIDAL[1], J. M. LOPEZ-VILLEGAS[1], (Senior Member, IEEE), AND JESUS A. DEL ALAMO[2], (Fellow, IEEE)

[1]RF Group, Department of Electronic and Biomedical Engineering, University of Barcelona, E-08028 Barcelona, Spain
[2]Microsystem Technology Laboratories, Massachusetts Institute of Technology, Cambridge, MA 02139, USA

Corresponding author: N. Vidal (nvidal@ub.edu)

This work was supported by the Spanish Secretariat of State for Research, Development and Innovation Under Project TEC2017-83524-R.

ABSTRACT The aim of this paper is to compare the performance of planar toroidal inductors and circular spiral inductors in multilayered technologies, in terms of achievable inductance density. New multi-winding toroidal inductor geometry is proposed to cover as much of the integration area as possible with the component footprint. The optimization of planar multi-winding toroidal inductors in multilayered substrates is investigated theoretically, and closed formulae are derived for their inductances as a function of geometrical parameters for any given value of the number of windings in the coil. The model obtained is validated experimentally and through electromagnetic simulation. Comparing the inductance of multi-winding toroidal inductors and compact spiral inductors allows us to update previously reported selection rules for the most suitable topology that leads to the most compact design.

INDEX TERMS Inductance calculation, inductor design, inductor optimization, inductor selection rules, multi-winding inductor, passive magnetic components, toroidal inductor.

I. INTRODUCTION

In our previous work [1], we presented an study of embedded toroidal inductors used in multilayered technologies. A model for such components was proposed and validated experimentally and through simulation. That model predicts the quasi-static inductance of the component as a function of geometrical parameters. An optimization process for the toroidal geometry was proposed to achieve the maximum inductance density. The toroidal inductor topology was compared with the planar spiral inductor topology in terms of achievable inductance density. In the frequency range from tens of MHz to a few hundred of MHz, it was not clear which of these two inductor topologies could achieve greater inductance. We stablished, to the best of our knowledge for the first time, selection criteria for choosing the most suitable inductor geometry for a given application.

Toroidal and planar spiral inductors were compared by selecting, a priori, the best candidates from each class. In the case of planar spiral inductors, the selection was clear. If we focus on achieving the highest possible inductance, the compact planar spiral inductor would be the best candidate of its kind. However, it is not clear which would be the best candidate of the toroidal inductors. In our previous work we choose as candidate the toroidal inductor with optimized geometry. Although with the optimized geometry we can achieve a maximum of the inductance, only the 63% of the available area is used to define the toroidal footprint. In the case of the planar spiral inductors all the available area can be used to define the metal spiral footprint. In accordance with this, it seems clear that the geometry of toroidal inductors can be improved further. Some work concerning the modeling, electromagnetic (EM) simulation, and microfabrication of toroidal inductors has been published since then by other authors, [2]–[5]. However, all of it considers the simple single-winding toroidal inductor geometry.

In this paper we explore new toroidal inductor geometries based on multiple windings. Our aim is to increase the coverage of the available integration area with the toroidal footprint as much as possible and to compare these new candidate geometries with the compact planar spiral inductor.

The paper is divided as follows. In Section II, we present the model of multi-winding toroidal inductors used in planar technologies. Closed formulae are derived for the

The associate editor coordinating the review of this manuscript and approving it for publication was Zhonglai Wang.

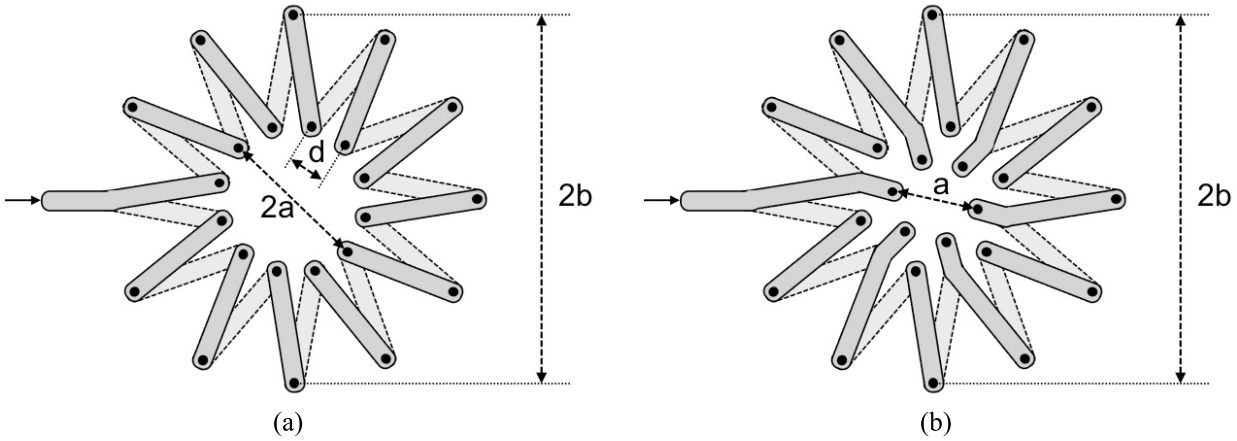

FIGURE 1. Implementation of a single-winding toroidal Inductor in multilayer technology (a) and proposed transformation into a double-winding toroidal inductor (b).

achievable inductance of these components as a function of the geometrical parameters for the general case of multi-winding toroidal inductor. Optimum inductor geometries that maximize the achievable inductance density are proposed for each value of the number of windings, m. Section III contains our experimental results and reports FEM simulations that confirm the accuracy of the proposed model. We used EMPro from Keysight Technologies Inc. as simulation tool. Section IV is then devoted to a comparison of the m-windings toroidal inductors with the planar spiral inductor, in terms of achievable inductance density. Here, the selection criteria of the most suitable inductor geometry for a given application are updated. Finally, the paper ends with our conclusions in Section V.

II. MULTI-WINDING TOROIDAL INDUCTOR MODEL FOR PLANAR TECHNOLOGIES

For the sake of completeness, before analyzing the inductance of alternative toroidal designs based on multi-winding geometries, it is useful to start with a quick review of the inductance analysis of a simple planar toroid, like that shown in Fig. 1a.

A. THE SINGLE-WINDING TOROID

The inductance of a single-winding toroidal inductor implemented using multilayered technology can be written as follows [6], [7]:

$$L = \mu \frac{N^2 h}{2\pi} ln\left(\frac{b}{a}\right) \tag{1}$$

where μ is the permeability of the medium inside the toroid, N is the number of turns, h is the substrate thickness, and a and b are the internal and external radii of the toroid, respectively.

Usually an additional term is included to account for the inductance of the circular loop around the center of the toroid that appears when the thickness, h, collapses to zero [8]. Considering this small contribution, L_o, we finally obtain:

$$L = \mu \frac{N^2 h}{2\pi} ln\left(\frac{b}{a}\right) + L_o \tag{2}$$

From Fig 1.a, we can see that:

$$N \approx \frac{2\pi a}{d} \tag{3}$$

where d is the minimum distance between vias in the inner circle of radius a.

After some geometrical considerations [1], expression (2) reduces to:

$$L = \mu \frac{V}{d^2} R^2 ln\left(\frac{1}{R^2}\right) + L_o \tag{4}$$

where, V is the total volume occupied by the toroid, which is equal to:

$$V = \pi b^2 h \tag{5}$$

and R is the ratio between the inner and outer radii of the toroid (i.e. $R = a/b$).

Neglecting the small contribution of L_o, it is straightforward to see that the inductance given by (4) shows a maximum for a value of the ratio, $R = R_{max}$, given by:

$$R_{max} = \frac{1}{\sqrt{e}} \tag{6}$$

and the maximum inductance value is equal to:

$$L_{max} = \frac{\mu V}{e d^2} \tag{7}$$

where, e, is the Euler number.

If we define the coverage of the integration area of the optimum toroid as the ratio between the area of the ring of radii a and b, and the area of the circle of radius, b, then we obtain a value of 63%. This means that it is still possible to further improve the toroidal inductor geometry.

B. THE DOUBLE-WINDING TOROID

The usual way to implement a double winding toroid consists of superposing both windings, one over the other. In planar multilayered technologies, this can be accomplished by performing the first windings using metal traces on internal layers of the substrate connected with internal vias. The second winding is then implemented using metal traces on the

top and bottom surfaces connected with stacked vias through the whole substrate. The higher the number of windings, the higher the number of layers we need to implement the component. The main drawback of this traditional implementation is its complexity when translated to a multilayered technology. A double winding toroid needs at least a three-layer substrate with internal vias. In the general case of an m-winding toroid, we would need a (2m-1)-layer substrate and internal stacked vias connecting all the metal levels. To avoid this drawback, we propose an alternative geometry to implement a double winding toroid. To construct it, we can use as our starting point the single winding toroid in Fig. 1a. Then, we move inwards half the number of via holes in the inner circle of radius a, until we reach a radius of $a/2$. In the new circle the distance between via holes remains equal to d. The last step consists of connecting the displaced via holes with their original location using top and bottom metal traces. The final result is shown in Fig. 1b, where we should note in the figure the presence of the inner ring of vias of diameter a, the middle ring of diameter $2a$, and the outer ring of diameter $2b$.

It is important to remark that this geometry can be implemented in any substrate, regardless of the number of layers it consists of. Moreover, the proposed geometry allows for better coverage of the available integration area with the toroid footprint. Finally, it can be extended in a straightforward way to the general case of an m-winding toroid.

Calculation of the inductance of the double-winding toroid requires the evaluation of the magnetic field strength, using the Ampere's law. To this end, we need to separate the radial coordinate, r, in two regions. The first one corresponds to the range $a/2 < \mathrm{r} < a$. In this case, only half the internal via holes are surrounded by the circular contour of radius, r. As a consequence, in the first region the Ampere's law can be expressed as:

$$\oint \vec{H}\vec{dl} = \frac{N}{2}I \tag{8}$$

where, I, is the current passing through every turn in the toroid.

The second region corresponds to the range $a < \mathrm{r} < b$. In this case, the internal via holes are all surrounded by the circular contour of radius r, and then:

$$\oint \vec{H}\vec{dl} = NI \tag{9}$$

By solving (8) and (9), a double expression for the magnetic field strength is obtained:

$$\left.\begin{aligned} \left|\vec{H}\right| &= \frac{NI}{4\pi r}\left(\tfrac{a}{2} < r < a\right) \\ \left|\vec{H}\right| &= \frac{NI}{2\pi r}\left(a < r < b\right) \end{aligned}\right\} \tag{10}$$

As well as for the magnetic flux density:

$$\left.\begin{aligned} \left|\vec{B}\right| &= \mu\frac{NI}{4\pi r}\left(\tfrac{a}{2} < r < a\right) \\ \left|\vec{B}\right| &= \mu\frac{NI}{2\pi r}\left(a < r < b\right) \end{aligned}\right\} \tag{11}$$

By integrating (11) in the cross section of the toroid, the total magnetic flux, Φ, can be written as:

$$\begin{aligned} \Phi &= \mu\frac{N^2I}{8\pi}h\int_{\left(a/2\right)}^{a}\frac{dr}{r} + \mu\frac{N^2I}{2\pi}h\int_{a}^{b}\frac{dr}{r} \\ &= \mu\frac{N^2I}{8\pi}h\,ln\,(2) + \mu\frac{N^2I}{2\pi}h\,ln\left(\frac{b}{a}\right) \end{aligned} \tag{12}$$

Accordingly, the inductance of the double-winding toroid is given by:

$$L = \mu\frac{N^2h}{2\pi}\left[\frac{ln\,(2)}{4} + ln\left(\frac{b}{a}\right)\right] \tag{13}$$

Expression (13) can be rewritten in terms of V, d and the ratio R, as follows:

$$L = \mu\frac{V}{d^2}R^2\left[\frac{ln\,(2)}{2} + ln\left(\frac{1}{R^2}\right)\right] \tag{14}$$

The inductance given by (14) also shows a maximum for a given value of the ratio R. In this case:

$$R_{max} = \frac{2^{1/4}}{\sqrt{e}} \tag{15}$$

and the maximum inductance value is equal to:

$$L_{max} = \frac{\mu V}{ed^2}2^{1/2} \tag{16}$$

By comparing (7) and (16), we can see that the maximum inductance value of the double-winding toroid is a factor $2^{1/2}$ greater than the inductance of the single winding toroid. This represents an improvement of about 41% in the inductance, while keeping the volume of the inductor constant. The maximum inductance of the double-winding toroid appears for the value R_{nax}, which is a factor of $2^{1/4}$ greater than that corresponding to the single-winding toroid (i.e., 0.72 instead of 0.61). Moreover, the coverage of the double-toroid footprint is equal to the 87% of the available integration area, instead of the 63% for the single-winding toroid. These facts can be observed graphically in Fig.2, where the inductance of the double-winding toroid, given by (14), is plotted together with that of the single-winding toroid, given by (4) (ignoring the contribution of,L_o). In both cases, the inductance values are normalized to the maximum of the single winding-toroid given by (7).

C. THE MULTIPLE-WINDING TOROID

The same procedure used to generate the double-winding toroid can be applied to generate a triple-, quadruple-, or in general a multiple-winding toroid structure (i.e., an m-winding toroid). At each step, half the number of via holes in the innermost circle are moved inwards until we reach a radius of $a/4$, $a/8$, or $a/2^{m-1}$, respectively.

Using the same reasoning as in the case of the double-winding toroid, we will arrive at the following expression for the inductance of a general, m-winding toroid:

$$L = \mu\frac{N^2h}{2\pi}\left[ln\,(2)\sum_{k=1}^{m-1}\left(\frac{1}{2^{2k}}\right) + ln\left(\frac{b}{a}\right)\right] \tag{17}$$

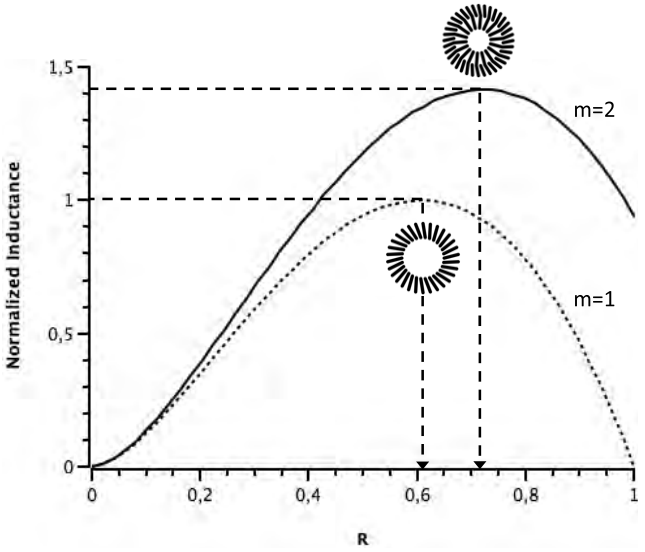

FIGURE 2. Plots of the normalized inductance of a single-winding toroid (m = 1) and double-winding toroid (m = 2) as a function of the geometrical ratio, *R*. In both cases the inductance is normalized to the maximum of the single-winding toroid. The insets are layout views of the optimal inductors in both cases.

The summation term in (17) is the sum of a geometric series. The first term in the series is $a_1 = 1/4$, and the ratio is, $t = 1/4$. Using the well-known formula for the sum of a geometric series consisting of n terms:

$$S = a_1 \frac{1 - t^n}{1 - t} \tag{18}$$

we obtain:

$$\sum_{k=1}^{m-1} \left(\frac{1}{2^{2k}}\right) = \frac{1}{3}\left[1 - \left(\frac{1}{4}\right)^{(m-1)}\right] \tag{19}$$

Finally, the inductance can be rewritten in terms of the volume occupied by the toroid V, the ratio R, and the minimum distance between vias d, as follows:

$$L = \mu \frac{V}{d^2} R^2 \left[\frac{2}{3}\left[1 - \left(\frac{1}{4}\right)^{(m-1)}\right] ln\,(2) + ln\left(\frac{1}{R^2}\right)\right] \tag{20}$$

Strictly speaking, (20) holds for, $m \geq 2$, and then includes as a particular case the double-winding toroid. Actually, by substituting $m = 2$ into (20), we obtain expression (14) corresponding to the double-winding toroid, as expected. However, if we substitute $m = 1$ into (20), we obtain expression (4), which correspond to the single-winding toroid, ignoring the term in, L_o. Accordingly, expression (20) holds for any planar toroid, regardless of the number of windings, m, it consists of.

The inductance given by expression (20) also shows a maximum for a given value of the ratio, R. In this case:

$$R_{max} = \frac{2^{\frac{1}{3}\left[1-\left(\frac{1}{4}\right)^{(m-1)}\right]}}{\sqrt{e}} \tag{21}$$

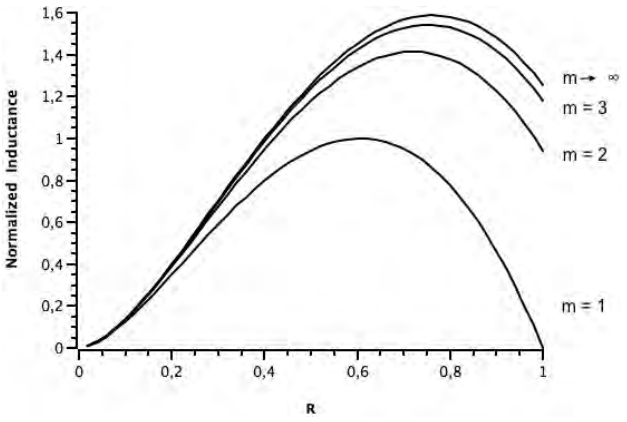

FIGURE 3. Plots of the normalized inductance of an *m*-winding toroid as a function of the geometrical ratio, *R*. For all values of *m*, the inductance is normalized to the maximum of the single-winding toroid (i.e., m = 1).

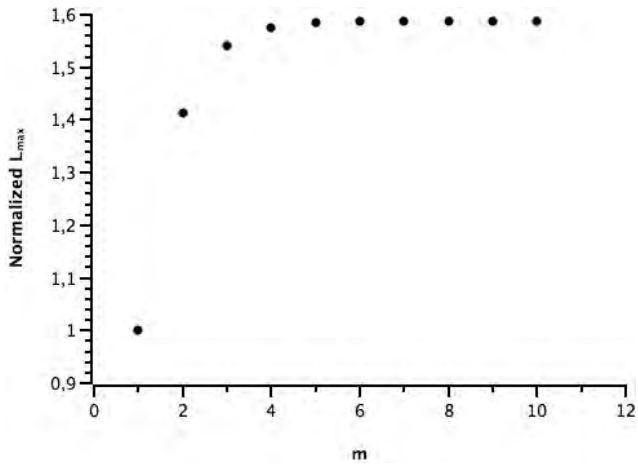

FIGURE 4. Maximum values of the normalized inductance of a *m*-winding toroid as a function of the number of winding, *m*. For all, *m*, values the inductance is normalized to the maximum of the single-winding toroid (i.e. m = 1).

and the maximum inductance value is equal to:

$$L_{max} = \frac{\mu V}{ed^2} 2^{\frac{2}{3}\left[1-\left(\frac{1}{4}\right)^{(m-1)}\right]} \tag{22}$$

Figs. 3, 4, and 5 summarize the results for the general case of an m-winding toroid. Fig. 3 shows the inductance given by (20) for different values of m, as a function of the ratio R. In all the cases, the inductance values are normalized to the inductance maximum corresponding to the case of a single-winding (i.e., $m = 1$). The normalized inductance maxima as a function of the number of windings, m, are shown in Fig. 4. Finally, the percentage of the available integration area covered by the optimum toroid footprint is shown in Fig. 5.

A close look at the figures indicates that the toroid inductance saturates very quickly as the number of windings increases. If we focus on the inductance maxima shown in Fig. 4, we can observe that the inductance when $m \geq 4$, is almost constant, and represents an improvement of about 59% with respect to the case of a single-winding. This is consistent with the fact that the area coverage in Fig. 5 is greater

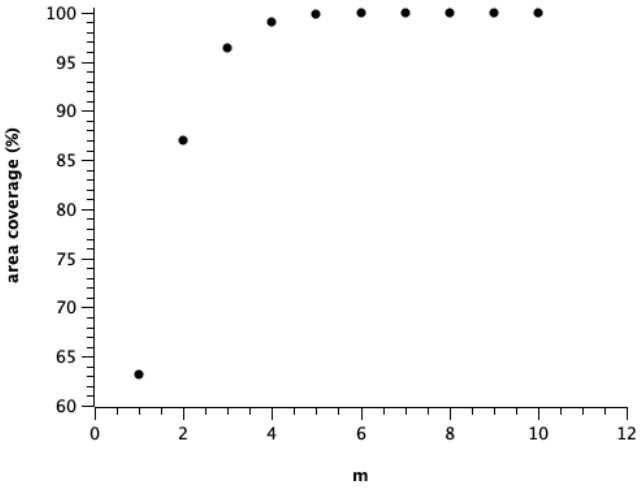

FIGURE 5. Percent of the available area covered by the optimum multi-winding toroid footprint as a function of the number of windings, *m*.

FIGURE 6. Example of fabricated multi-winding toroidal inductors. In the top row we can see three double-winding samples, corresponding, from left to right, to: $N = 24$, 32 and 36, respectively. On the bottom row we can see three triple-winding samples, corresponding to: $N = 32$, 36 and 40.

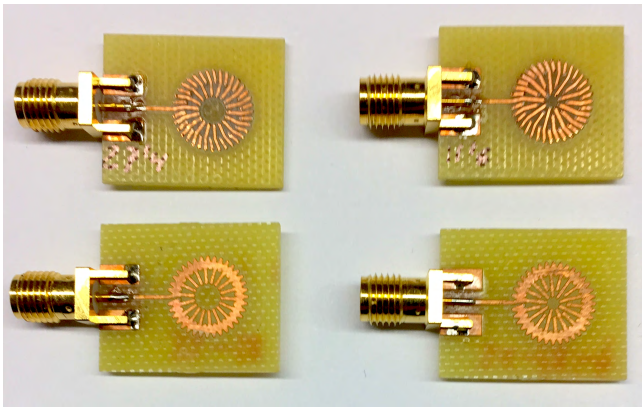

FIGURE 7. At the top, from left to right, double- and triple-winding toroidal inductors corresponding to, $N = 36$. At the bottom, the same inductors after merging the upper and lower metal layers of the toroid on the top surface of the PCB.

than 99% when $m \geq 4$. In practice, a good tradeoff between design complexity and inductance improvement would be the triple-winding toroid (i.e., $m = 3$). In this case, the inductor geometry is not too complicated, the inductance improvement at the maximum is equal to 54%, with respect to the case of a single-winding, and the available area coverage is 96.4%.

III. EXPERIMENTAL VALIDATION

In our previous work, we used a set of samples consisting of single-winding toroidal inductors, planar spiral inductors, and test structures for de-embedding purposes [1]. Different substrate materials and thicknesses were also considered.

In order to verify the accuracy of the proposed model of a multi-winding toroidal inductor in multilayered planar technologies, we need to complete our original set of samples by including at least double- and triple-winding toroidal inductors. Fig. 6 shows an example of these multi-winding structures. We fabricated double- and triple-winding toroidal inductors using a standard PCB process. The design of these components was done using the Advanced Design System (ADS) environment from Keysight Technologies Inc. In order to be consistent with the previous set of samples, we applied the same geometrical constrains. These are: substrate thickness, h = 1.57 mm; external radius, b = 4.7 mm; minimum distance between vias, d = 0.6 mm; metal trace width, w = 0.45 mm; minimum distance between metal traces, s = 0.15 mm; and the metal thickness t = 35μm. As with the single-winding toroid, these multi-winding structures are also affected by the residual inductance, Lo, which appears in (4), but is also implicit in (14) and (20). In order to be able to remove this contribution, we need to know the inductance when the substrate thickness, h, trends to zero. To this end, additional samples were fabricated by merging the top and bottom metal layers of the toroid on the top surface of the PCB. Fig. 7 shows the result of this procedure.

For the sake of consistency, to characterize the multi-winding toroidal inductors, we used the same experimental and simulation setups used for the single-winding toroidal inductors [1]. Basically, S parameters, either measured or simulated using finite element method (FEM), are used as raw data to determine the equivalent inductance and quality factor for all the structures, including those corresponding to $h \approx 0$. A custom calibration kit is used to remove the effect of the SMA connectors and pads from the experimental measurements. Finally, the equivalent inductance values of the multi-winding toroidal inductors are corrected by subtracting the quasi-static inductance values corresponding to the same structures when $h \approx 0$. Fig. 8 shows the

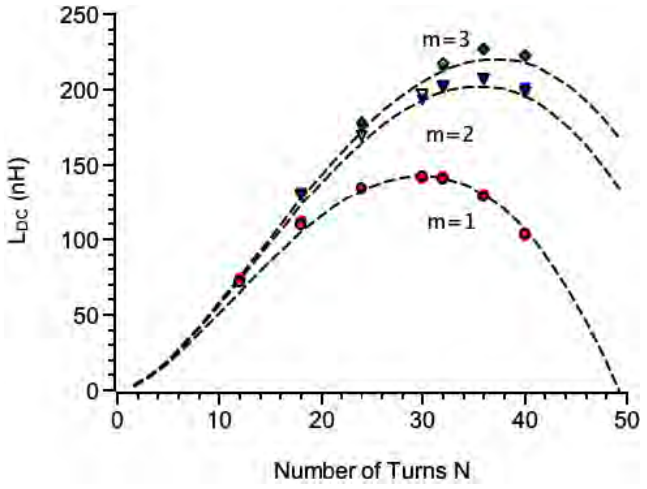

FIGURE 8. Corrected values of the quasi-static inductance of multi-winding toroidal inductors after removal of the inductance, L_0. Solid symbols correspond to experimental measurements. Outlined symbols correspond to FEM simulation results. Circles are results of single-windings ($m = 1$); triangles and diamonds of double and triple windings (m = 2,3), respectively. Dashed lines are the theoretical curves.

corrected values of the quasi-static inductance for single-, double- and triple-winding toroidal inductors (m = 1, 2 and 3, respectively), together with the theoretical curves given by (20). We notice the good agreement between the data and theory without using any fitting parameter.

IV. M-WINDING TOROIDAL VS SPIRAL INDUCTORS

For comparison purposes, we used the analytical expression for the inductance of a planar spiral inductor reported in [9], in the particular case of a compact circular spiral. After some redefinition of the geometrical parameters, to fit those used for the toroidal inductors, the inductance of a circular spiral inductors can be written as follows [1]:

$$L = \frac{k}{\pi}\frac{\mu S}{d^2}b \tag{23}$$

The parameter k is a constant equal to 0.55, and S is the total area occupied by the spiral, which is given by:

$$S = \pi b^2 \tag{24}$$

Also, in (23), d stands for the pitch between the turns of the circular spiral.

Let us now compare the inductance of the compact spiral, given by (23), with the maximum inductance of an m-winding toroid, given by (22). Considering that, $V = Sh$, it is easy to see that the ratio between the inductances is proportional to the aspect ratio of their cross section, b/h.

$$\frac{L_{spiral}}{L_{m-toroid}} = \gamma_m \frac{b}{h} \tag{25}$$

and the proportionality constant, γ_m, is equal to:

$$\gamma_m = \frac{ek}{\pi} 2^{-\frac{2}{3}\left[1-\left(\frac{1}{4}\right)^{(m-1)}\right]} \tag{26}$$

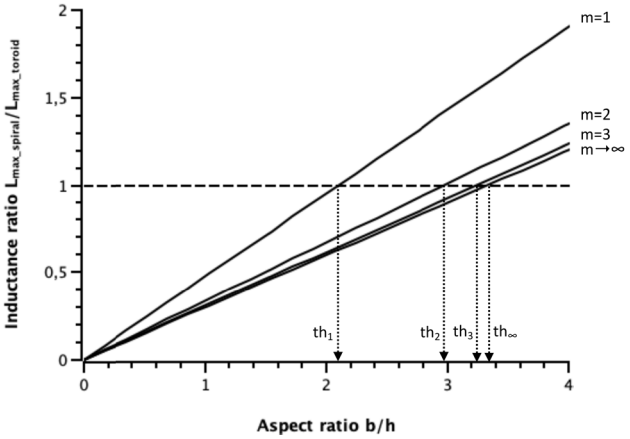

FIGURE 9. Planar spiral inductance over optimal toroid inductance as a function of the inductor aspect ratio, b/h.

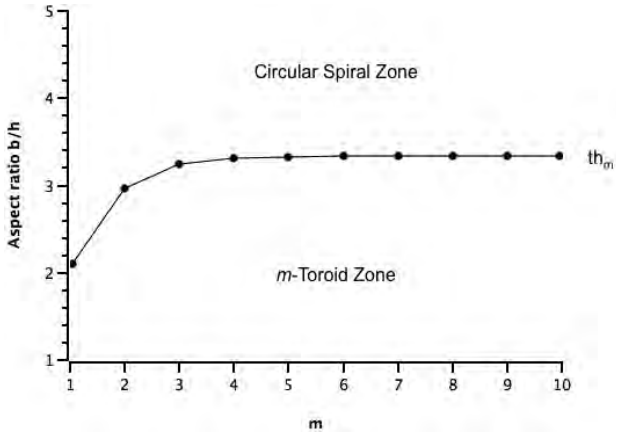

FIGURE 10. Selecting thresholds plot in the plane: inductor aspect ratio, b/h, number of wingdings of the toroid, m. The zones where a particular geometry outperforms are also indicated on the graph.

Fig. 9 shows the inductance ratio as a function of b/h for different values of m. For any given value of m, the point of intersection with the dashed line, at an inductance ratio equal to unity, determines a threshold, th_m. From (25), it is straightforward to see that, $th_m = 1/\gamma_m$.

A close look at Fig. 9 indicates that for a given value of m, when $b/h < th_m$, the m-winding toroid outperforms the circular planar spiral in terms of achievable inductance. In contrast, when, $b/h > th_m$, the circular planar spiral outperforms the m-winding toroid.

Fig. 10 shows the values of the thresholds th_m, as a function of m. In accordance with the preceding considerations, the range of aspect ratios has been divided in two zones for each value of m. The "Circular Spiral Zone" and the "m-Toroid Zone", depending on which geometry is the best choice in terms of achievable inductance. The threshold between zones saturates very quickly with increasing m, to a value of the aspect ratio of about 3.33.

In order to verify the accuracy of the updated selection criteria, we have fabricated a new set of samples consisting

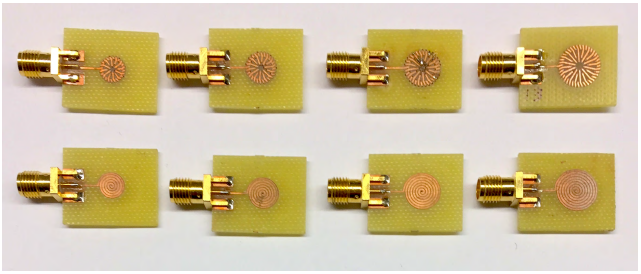

FIGURE 11. Example of fabricated inductors. In the top row we can see four triple-winding samples, corresponding to diferent values of the external radius, *b*. In the bottom row we can see four circular spiral samples, corresponding to the same external sizes.

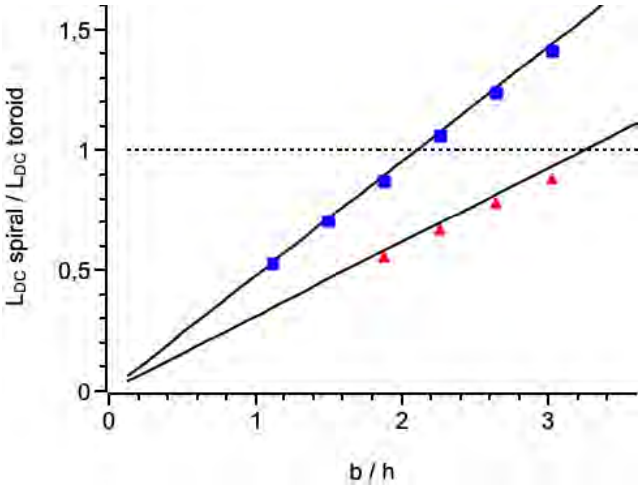

FIGURE 12. Quasi-static inductance ratio as a function of the aspect ratio, *b/h*. Squares and triangles correspond to single- and triple-winding toroid results, ($m = 1$ and $m = 3$), respectively. Continuous lines correspond to the theoretical behavior.

of triple-winding toroidal inductors. Each sample corresponded to a different value of the external radius, b. In all cases, the inductor footprint was that of the optimum design. These samples were compared with the same circular spiral inductors we used in our previous work, where the comparison was done only with single-winding toroidal inductors. Fig. 11, shows some of the samples used for the inductance comparison. Fig. 12 shows a plot of the ratio between the quasi-static inductance of spiral and optimum toroid inductors as a function of the aspect ratio, b/h. To obtain the quasi-inductance ratios at exactly the same value of b/h, data corresponding to the spiral inductors were fitted to a third order polynomial and then interpolated. Single- and triple-winding toroidal inductors (i.e., $m = 1$ and $m = 3$, respectively) were compared with the same spiral inductors. In the figure, the theoretical dependences derived from (25) and (26) are also shown. We have to remark on the very good agreement observed between experimental measurements and theory.

V. CONCLUSION

In this work, we present a general model for the inductance of multi-winding toroidal inductors in multilayered technologies. The model is derived from an EM analysis of the multi-winding geometry and predicts the whole quasi-static inductance of the component. It also allows optimization of the inductor geometry to achieve the maximum inductance density for any given number of windings, m. The proposed model has been validated by experimental measurements and EM simulations using FEM. The selection criteria, established in our previous work, to decide whether to use a planar spiral inductor or a toroidal inductor for a given application have been updated to account for multi-winding geometries. As a result, new threshold values for the aspect ratio of the components have been found, for any given value of the number of windings, m. An upper limit on the aspect ratio of $b/h \approx 3.33$ has been obtained. If the aspect ratio of the inductor is greater than this upper threshold, the planar spiral inductor outperforms any multi-winding toroidal inductor. Conversely, if the aspect ratio is smaller than the upper threshold there is at least one multi-winding toroidal inductor that outperforms the planar spiral inductor. In accordance with this, if we consider an integration technology consisting of a semiconductor bulk with thin inter-metal dielectric layers on it, the aspect ratio for most components will be very large, and the natural choice for implementing inductors would be a planar spiral geometry. In contrast, when using integration technologies with thick inter-metal dielectrics or when using multilayered substrates, such as LTCC or PCB, the choice is not so clear. It is in these latter cases that, depending on the inductance value required, the application of the updated selection rules reported in this work will give the optimum multi-winding toroidal inductor design. Further work is in progress to compare other characteristic parameters of these structures, such as the substrate coupling, and thereby to establish additional selection rules. A planar spiral inductor generates a magnetic field which penetrates deep into the substrate. This could be a source of magnetically induced losses leading to a strong decrease of the quality factor of the component. In the case of the multi-winding toroidal inductors, the magnetic field is confined inside the component; moreover, it is parallel to the substrate. Accordingly, very little coupling is expected, with no relevant impact on the quality factor of the component. This difference in behavior should also be considered when deciding on the inductor topology to use.

REFERENCES

[1] J. M. Lopez-Villegas, N. Vidal, and J. A del Alamo, "Optimized toroidal inductors versus planar spiral inductors in multilayered technologies," *IEEE Trans. Microw. Theory Techn.*, vol. 65, no. 2, pp. 423–431, Feb. 2017.

[2] G. Zulauf, W. Liang, and J. Rivas-Davila, "A unified model for high-power, air-core toroidal PCB inductors," in *Proc. 18th IEEE Workshop Control Modeling Power Electron.*, Jul. 2017, pp. 1–8.

[3] E. D. Langlois, T. C. Monson, D. L. Huber, and J. Watt, "Finite element modeling of nanoscale-enabled microinductors for power electronics," *J. Mater. Res.*, vol. 33, no. 15, pp. 2223–2233, Aug. 2018.

[4] H. T. Le, Y. Nour, A. Han, F. Jensen, Z. Ouyang, and A. Knott, "Micro-fabricated air-core toroidal inductor in very high-frequency power converters," *IEEE J. Emerg. Sel. Topics Power Electron.*, vol. 6, no. 2, pp. 604–613, Jun. 2018.

[5] H. T. Le, Y. Nour, Z. Pavlovic, C. O'Mathúna, A. Knott, F. Jensen, A. Han, S. Kulkarni, and Z. Ouyang, "High-Q Three-dimensional microfabricated magnetic-core toroidal inductors for power supplies in package," *IEEE Trans. Power Electron.*, vol. 34, no. 1, pp. 74–85, Jan. 2019.
[6] E. B. Rosa, "The self-inductance of a toroidal coil of rectangular section," *Bull. Bureau Standards*, vol. 4, no. 1, pp. 141–148, 1907.
[7] J. Pejtersen and A. Knott, "Design and measurement of planar toroidal transformers for very high frequency power applications," in *Proc. IEEE 7th Int. Power Electron. Motion Control Conf.*, Jun. 2012, pp. 688–692.
[8] C. R. Sullivan, W. Li, S. Prabhakaran, and S. Lu, "Design and fabrication of low-loss toroidal air-core inductors," in *Proc. IEEE Power Electron. Spec. Conf.*, Jun. 2007, pp. 1754–1759.
[9] S. S. Mohan, M. Del M. Hershenson, S. P. Boyd, and T. H. Lee, "Simple accurate expressions for planar spiral inductances," *IEEE J. Solid-State Circuits*, vol. 34, no. 10, pp. 1419–1424, Oct. 1999.

N. VIDAL received the Ph.D. degree in physics from the University of Barcelona, Spain, in 1995, where she is currently an Associate Professor and is a member of the Group of Excellence for Radio Frequency Components and Systems. Her current research interests include passive components for RF applications, antenna design for biomedical applications, and electromagnetic propagation-related issues.

J. M. LOPEZ-VILLEGAS (M'93–SM'03) received the Ph.D. degree in physics from the University of Barcelona, Barcelona, Spain, in 1990, where he is currently the Director of the Group of Excellence for Radio Frequency Components and Systems and a Full Professor with the Department of Electronic and Biomedical Engineering. His research interests include centered in the design, optimization, and test of RF components, circuits and systems performed using silicon, multilayered technologies, like multichip modules and low-temperature co-fired ceramics, and 3-D printing, use of 3-D simulators for electromagnetic analysis of RF components, circuits, and systems, the analysis of electromagnetic compatibility and electromagnetic interference problems, and the interaction of electromagnetic energy with biological tissues. He is particularly interested in the modeling and optimization of integrated inductors and transformers for general RF applications, and in particular for the development of new homodyne transceiver architectures based on injection-locked oscillators.

JESUS A. DEL ALAMO (S'79–M'85–SM'92–F'06) received theTelecommunications Engineer degree from the Polytechnic University of Madrid in 1980 and the M.S. and Ph.D. degrees in electrical engineering from Stanford University in 1983 and 1985, respectively. From 1985 to 1988, he was with NTT LSI Laboratories, Atsugi, Japan. Since 1988, he has been with the Department of Electrical Engineering and Computer Science, Massachusetts Institute of Technology, where he is currently a Donner Professor and the Director of the Microsystems Technology Laboratories. He was an NSF Presidential Young Investigator. His current research interest includes microelectronics technologies for communications and logic processing. He is a member of the Royal Spanish Academy of Engineering and a fellow of the American Physical Society. He was the recipient of the Intel Outstanding Researcher Award in Emerging Research Devices, the Semiconductor Research Corporation Technical Excellence Award, and the IEEE EDS Education Award. He is a former Editor of the IEEE ELECTRON DEVICE LETTERS.